Metals **2015**, *5*, 484-503; doi:10.3390/met5020484

OPEN ACCESS

metals

ISSN 2075-4701

www.mdpi.com/journal/metals

Article

Effects of Annealing on the Martensitic Transformation of Ni-Based Ferromagnetic Shape Memory Heusler Alloys and Nanoparticles

Tina Fichtner [1], Changhai Wang [1], Aleksandr A. Levin [1], Guido Kreiner [1], Catalina Salazar Mejia [1], Simone Fabbrici [2,3], Franca Albertini [2] and Claudia Felser [1,*]

[1] Max-Planck-Institute for Chemical Physics of Solids (MPI CPFS), Noethnitzer Str. 40, DE-01187 Dresden, Germany; E-Mails: tina.fichtner@cpfs.mpg.de (T.F.); changhai.wang@cpfs.mpg.de (C.W.); alexander.levin@cpfs.mpg.de (A.A.L.); guido.kreiner@cpfs.mpg.de (G.K.); catalina.salazar@cpfs.mpg.de (C.S.M.)

[2] Institute of Materials for Electronics and Magnetism, National Research Council (IMEM-CNR), Parco Area delle Scienze 37/A, I-43124 Parma, Italy; E-Mails: simone.fabbrici@imem.cnr.it (S.F.); franca.albertini@imem.cnr.it (F.A.)

[3] Laboratory of Micro and Submicro Enabling Technologies for Emilia-Romagna (MIST E-R), via Gobetti 101, I-40129 Bologna, Italy

* Author to whom correspondence should be addressed; E-Mail: claudia.felser@cpfs.mpg.de; Tel.: +49-351-4646-3004; Fax: +49-351-4646-3002.

Academic Editor: Kurt R. Ziebeck

Received: 20 February 2015 / Accepted: 12 March 2015 / Published: 25 March 2015

Abstract: We report on the effects of annealing on the martensitic phase transformation in the Ni-based Heusler system: $Mn_{50}Ni_{40}Sn_{10}$ and $Mn_{50}Ni_{41}Sn_9$ powder and $Co_{50}Ni_{21}Ga_{32}$ nanoparticles. For the powdered $Mn_{50}Ni_{40}Sn_{10}$ and $Mn_{50}Ni_{41}Sn_9$ alloys, structural and magnetic measurements reveal that post-annealing decreases the martensitic transformation temperatures and increases the transition hysteresis. This might be associated with a release of stress in the $Mn_{50}Ni_{40}Sn_{10}$ and $Mn_{50}Ni_{41}Sn_9$ alloys during the annealing process. However, in the case of $Co_{50}Ni_{21}Ga_{32}$ nanoparticles, a reverse phenomenon is observed. X-ray diffraction analysis results reveal that the as-prepared $Co_{50}Ni_{21}Ga_{32}$ nanoparticles do not show a martensitic phase at room temperature. Post-annealing followed by ice quenching, however, is found to trigger the formation of the martensitic phase. The presence of the martensitic transition is attributed to annealing-induced particle growth and the stress introduced during quenching.

Keywords: phase transitions; magnetism; X-ray and electron scattering

1. Introduction

Heusler alloys that belong to the ferromagnetic shape memory alloys (FSMAs) have been a fascinating class of materials since they were reported by Ullakko *et al.* [1] two decades ago. FSMAs are ferromagnetic and show a magnetic field-induced martensitic transformation. Most shape memory Heusler alloys contain Ni. Those with Mn and Ga, In, Sn and Sb [2–6] are the most investigated compounds. They are characterized by large magnetic field-induced strain [7,8], large magneto-resistance [9,10] and a significant magnetocaloric effect [11–13].

Mn-rich Ni- and Mn-based Heusler alloys have recently become the focus of research owing to their high localized magnetic moment of 4.0 μ_B at the Mn atom and their potential for enhanced magnetocaloric properties [11,14]. Mn-rich $Mn_{50}Ni_{50-x}Sn_x$ Heusler compounds were reported to show a significant exchange bias field [15], large magnetic entropy change [16,17], small thermal hysteresis and large magnetization change at the martensitic transformation [18]. However, little attention has been paid to the effect of annealing on those compounds.

The influence of post-annealing on the martensitic transformation of Ni-rich Ni-Mn-Sn alloys has been studied by Schagel, McCallum and Lograsso [19] on bulk material and Xuan *et al.* [20] on ribbons. Schagel, McCallum and Lograsso [19] reported that the magnetization change at the martensitic transformation is dependent on the annealing time. After an annealing time of approximately four weeks at 1223 K, they observed the highest magnetization change during the martensitic transformation and no overlap of the transition temperatures. Xuan *et al.* [20], on the other hand, reported that annealing of ribbons resulted in an increase in the reverse martensitic transition temperature (T_A) from 230 K (melt-spun) to 265 K (annealed at 1173 K). Concomitantly, the Curie temperature of the austenite T_C^A increased from T_C^A = 270 K (melt-spun) to T_C^A = 275 K (annealed at 1173 K). The reason for the increase of T_A and T_C^A is attributed to stress and structural relaxation during post-annealing.

In addition to these well-investigated Ni- and Mn-based compounds, other FSMAs have been studied, *i.e.*, Ni-Fe-Ga [21–23], Co-Ni-Al [24,25] and Co-Ni-Ga [26–29]. The Co-Ni-Ga Heusler system was intensively studied as a promising alternative to Ni-Mn-Ga alloys, especially for high-temperature shape memory device applications [30–37]. Co-Ni-Ga compounds generally exhibit a dual-phase microstructure: a parent phase (β) and a non-transformable secondary phase (γ). The ductile Ni-rich γ-phase enhances the overall workability of the Co-Ni-Ga alloys. Owing to the absence of a modulated or layered structure in martensite, the magnitude of the magnetic field-induced strain (MFIS) in Co-Ni-Ga alloys is normally much smaller than that of Ni-Mn-Ga alloys [38]. Even so, Co-Ni-Ga compounds are still promising candidates as classical thermally-triggered shape memory materials.

The effects of annealing on the structural and magnetic phase transformation of Co-Ni-Ga compounds have been reported for bulk and ribbon samples [27,39,40]. Liu *et al.* [27] studied the effects of annealing temperature and cooling conditions on the structure and martensitic transformation of bulk $Co_{46}Ni_{27}Ga_{27}$. It was found that the martensitic transformation temperature increased monotonically

with increasing annealing temperature and quenching rate. The precipitation of the non-transformable γ-phase can be avoided if the annealing temperature is higher than 1393 K. Sarma *et al.* [39] observed a similar correlation between the annealing temperature and the martensitic transformation in $Co_{47}Ni_{23}Ga_{30}$ ingots. It was also found that a higher annealing temperature significantly increased the Curie temperature and moderately decreased the amount of the γ-phase. Dai *et al.* [40] found that annealing of the $Co_{50}Ni_{20}Ga_{30}$ ribbons at 673 K suppressed the martensitic transformation and significantly influenced their magnetic properties. Post-annealing at higher temperatures (>873 K) and quenching recovered the martensitic phase transition of the $Co_{50}Ni_{20}Ga_{30}$ ribbons. This was attributed to the elimination of the precipitates and weight fractional variations of the transformable β-phase and the non-transformable γ-phase by the post-annealing.

To our knowledge, no study on the effect of annealing on the martensitic phase transformation of nanostructured $Co_{50}Ni_{21}Ga_{32}$ nanoparticles, and $Mn_{50}Ni_{40}Sn_{10}$ and $Mn_{50}Ni_{41}Sn_9$ powder has been conducted. Herein, we report on the synthesis and annealing-dependent martensitic phase transformation of $Co_{50}Ni_{21}Ga_{32}$ nanoparticles, and powdered $Mn_{50}Ni_{40}Sn_{10}$ and $Mn_{50}Ni_{41}Sn_9$ alloys.

This paper is divided into two parts. First, we present the results for the $Mn_{50}Ni_{40}Sn_{10}$ and $Mn_{50}Ni_{41}Sn_9$ powder, followed by the results for the $Co_{50}Ni_{21}Ga_{32}$ nanoparticles. In the following, the as-prepared powder is that which resulted from the melting of the elements, performing a heat treatment with quenching and grinding in a mortar. The post-annealed powder is that subjected to a subsequent annealing procedure without quenching. CNG_AS denotes the as-prepared $Co_{50}Ni_{21}Ga_{32}$ nanoparticles and CNG_AQ the annealed and quenched $Co_{50}Ni_{21}Ga_{32}$ nanoparticles.

2. Results and Discussion

2.1. $Mn_{50}Ni_{40}$ Sn_{10} and $Mn_{50}Ni_{41}$ Sn_9 Powder

2.1.1. Microscopic Analysis

In order to investigate the effect of annealing on the martensitic transformation in Mn-rich Ni-based FSMAs, the alloys $Mn_{50}Ni_{40}Sn_{10}$ and $Mn_{50}Ni_{41}Sn_9$ were synthesized and characterized by optical and scanning electron microscopy (SEM) with energy dispersive X-ray spectroscopy (EDXS). Figure 1 shows the bright field and back-scattered electron micrographs of $Mn_{50}Ni_{40}Sn_{10}$. Both methods exhibit a matrix with an embedded secondary phase, which indicates a two-phase material; the composition of the main phase is $Mn_{47.0}Ni_{41.8}Sn_{11.2}$, and that of the secondary phase is $Mn_{68.9}Ni_{28.8}Sn_{2.3}$. The errors of the SEM/EDX analysis are estimated with ± 0.5 at%. This secondary phase, which contains a high amount of Mn, is described as the γ-phase in the literature [41]. Liu *et al.* [41] reported the presence of this phase in Ni-Fe-Co-Ga alloys and ascribed the absence of martensitic transformation in the altered austenitic matrix to the γ-phase.

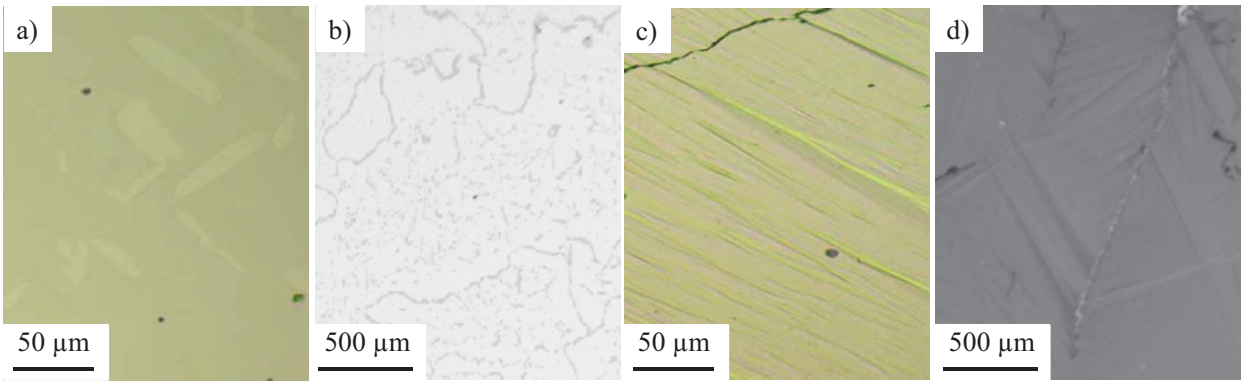

Figure 1. Optical and SEM/EDXS-micrographs of $Mn_{50}Ni_{40}Sn_{10}$: (**a**) bright field and (**b**) back-scattered electron images; (**c**) bright field and (**d**) secondary electron images of $Mn_{50}Ni_{41}Sn_9$.

In the current study, it was found that a tiny variation of the composition of approximately 1 at% changes the microstructure completely, as shown for $Mn_{50}Ni_{41}Sn_9$ in the bright field image in Figure 1c and the secondary electron image in Figure 1d. This microstructure, with its martensitic domains and needle-like shapes, reveals a martensitic structure at room temperature (r.t.), which confirms a martensitic transformation. For this alloy, SEM/EDXS analysis revealed a composition of $Mn_{48.9}Ni_{41.7}Sn_{9.4}$, which is close to the nominal composition.

Additionally, inductively-coupled plasma-optical emission spectroscopy (ICP-OES) analysis was performed to verify the powder compositions. The results showed that the mean analytical composition of the alloy $Mn_{50}Ni_{40}Sn_{10}$ was $Mn_{49.9(1)}Ni_{40.2(1)}Sn_{10.0(1)}$, which is close to the nominal composition. For the compound $Mn_{50}Ni_{41}Sn_9$, an analytical composition of $Mn_{49.7(1)}Ni_{41.3(1)}Sn_{9.0(1)}$ was obtained. Therefore, the analytical compositions of these alloys are in good agreement with their nominal compositions.

2.1.2. Phase Analysis

To support the results from the microstructure analysis of $Mn_{50}Ni_{40}Sn_{10}$, X-ray diffraction (XRD) analysis was performed. Figure 2 shows the r.t. XRD patterns of the as-prepared and the post-annealed powders. Most of the Bragg reflections of the XRD pattern of Figure 2a can be attributed to a cubic Heusler-type crystal structure with the space group (sg) 225 ($Fm\bar{3}m$) and a lattice parameter a = 5.997(2) Å. This result indicates an austenitic crystal structure at r.t.

However, in Figure 2a, a second phase could be referred to the diffraction pattern, which belongs to the fcc γ-phase of Mn-Ni with a lattice parameter of a = 3.724(4) Å. Both determined crystal structures support the EDXS analysis, which resulted in analytical compositions of $Mn_{47.0}Ni_{41.8}Sn_{11.2}$ and $Mn_{68.9}Ni_{28.8}Sn_{2.3}$. This γ-phase is known to be present in Ni-based Heusler alloys, as reported in the literature [41–43], appearing as a secondary phase next to the austenite. Thus, the γ phase is attributed to a reduction of the magnetization change during the martensitic transformation and to a vanishing of the martensitic transformation.

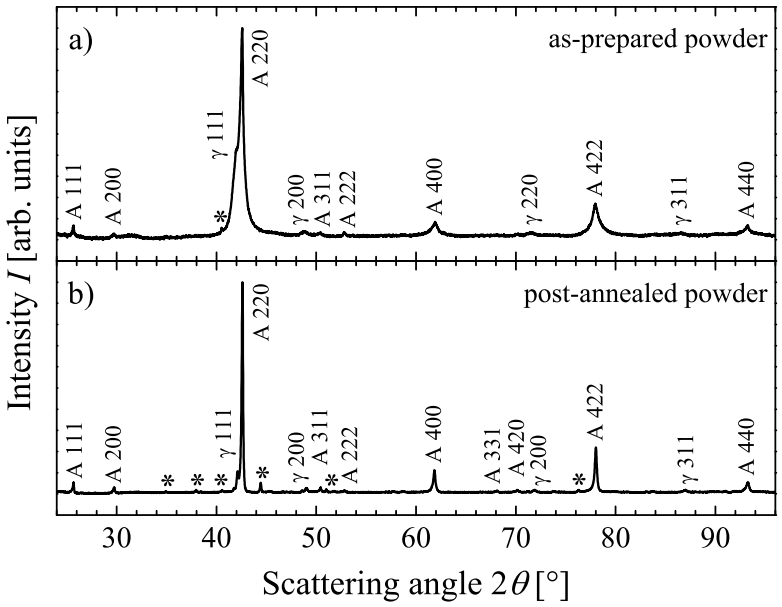

Figure 2. XRD pattern of $Mn_{50}Ni_{40}Sn_{10}$ at r.t. for (**a**) as-prepared and (**b**) post-annealed powders. "A" indicates the austenite and "γ" the fcc Mn-Ni phase. Mn-rich impurities are labeled by asterisks.

After annealing the powder in order to reduce the stress, the Bragg reflections shown in Figure 2b are much sharper, resulting again in a cubic Heusler-type crystal structure $Fm\bar{3}m$ with a lattice parameter of a = 5.993(1) Å and an fcc γ-phase with a lattice parameter of a = 3.711(1) Å.

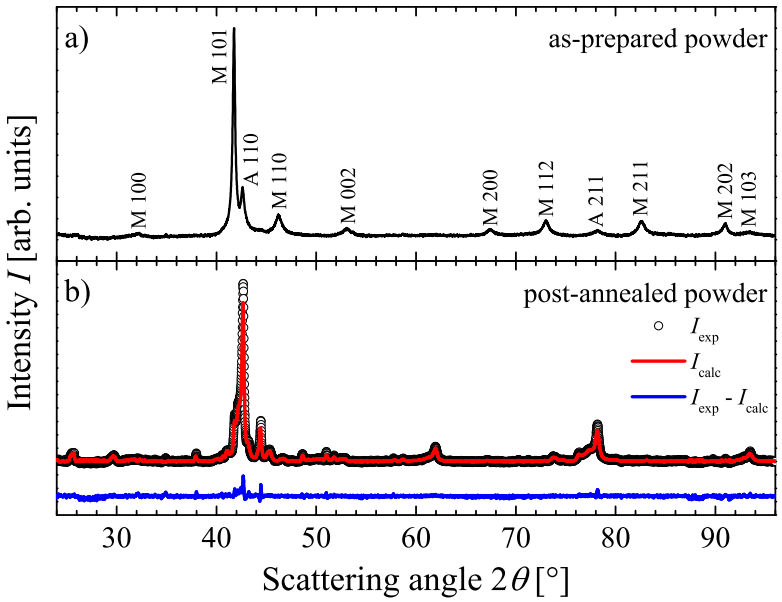

Figure 3. XRD pattern of $Mn_{50}Ni_{41}Sn_9$ at r.t. for (**a**) as-prepared and (**b**) post-annealed powders. "A" indicates the austenite and "M" the martensite. Results of Le Bail fitting are shown in (**b**) (R_{wp} = 10%).

Concerning $Mn_{50}Ni_{41}Sn_9$ (Figure 3a), the Bragg reflections are significantly different from those of the $Mn_{50}Ni_{40}Sn_{10}$ alloy, probably due to a slightly lower Sn-content. At r.t. $Mn_{50}Ni_{41}Sn_9$ reveals a martensitic tetragonal crystal structure ($P4/mmm$, CuAu structure type, sg: 123) with lattice parameters of a = 2.773(1) Å and c = 3.444(2) Å. The corresponding c/a-ratio is approximately 1.24. In addition to this martensite, there is also an austenitic phase with a lattice parameter of a = 2.990(1) Å ($Im\overline{3}m$, tungsten structure type, sg: 229). A crystal structure with a higher order (CsCl structure type, $Pm\overline{3}m$, sg: 221) is indicated by a tiny Bragg reflection at $2\theta = 53.72°$, which is not indexed to the tungsten structure type.

After recrystallization of the post-annealed powder, the diffraction pattern becomes more complex. The diffraction pattern could be indexed to a $7M$ superstructure cell with lattice parameters of a = 4.304(5) Å, b = 5.984(5) Å, and c = 42.223(7) Å and β = 93.97(2)°, using a Le Bail fitting, which is shown in Figure 3b. These lattice parameters are similar to those of the superstructure cell in the Ni-Mn-Ga FMSA [44–46]. It should be noted that owing to strong reflection overlap in the Le Bail fitting, it is not possible to exclude the presence of the austenitic phase at r.t. in this sample.

2.1.3. Magnetic Properties

The magnetic properties were determined by magnetometry. Figure 4a shows the temperature-dependent magnetization analysis of the as-prepared $Mn_{50}Ni_{40}Sn_{10}$ powder with applied fields, $\mu_0 H$, of 0.1, 2 and 7 T in the field cooling and field heating modes, starting from 400 K. Concerning $Mn_{50}Ni_{40}Sn_{10}$ at $\mu_0 H$ = 0.1 T, three phase transformations are shown (from low to high temperature): (i) a magnetic transformation in the martensite with a Curie temperature, T_C^M; (ii) a magnetostructural transformation with a martensitic start temperature, M_s, a martensitic finish temperature, M_f, and an inflection point of the martensitic transition, T_M; and (iii) a magnetic transformation in the austenite with a Curie temperature, T_C^A. Thus, $Mn_{50}Ni_{40}Sn_{10}$ possesses martensitic transformation temperatures of M_s = 221 K, M_f = 175 K and T_M = 202 K and two Curie temperatures for the martensite and austenite phases of T_C^M = 144 K and T_C^A = 274 K, respectively. The martensitic transformation temperatures are below r.t. Therefore, the austenite phase found at r.t. from the XRD analysis is verified.

Additionally, the magnetization change during the martensitic transformation is 30 $Am^2\ kg^{-1}$, which indicates a different magnetic order between the martensite and austenite. Thus, the martensite orders ferrimagnetically, whereas the austenite orders ferromagnetically.

The magnetization change at $\mu_0 H$ = 7 T is increased by 55% and T_M decreases with further increasing of $\mu_0 H$ from $T_{M,0.1T}$ = 202 K to $T_{M,7T}$ = 189 K, which is ascribed to a field-induced first order magnetostructural transformation. A reduced thermal hysteresis ΔT_{Hyst} of 7 K, as compared to other Heusler alloys [11,14], was obtained, which is comparable with the results published by Han [12] and Ma *et al.* [18]. However, ΔT_{Hyst} remains constant with increasing of $\mu_0 H$, resulting in a possible reduction in energy consumption in magnetocaloric applications, contrary to Ni-rich Ni- and Mn-based Heusler alloys [11,14].

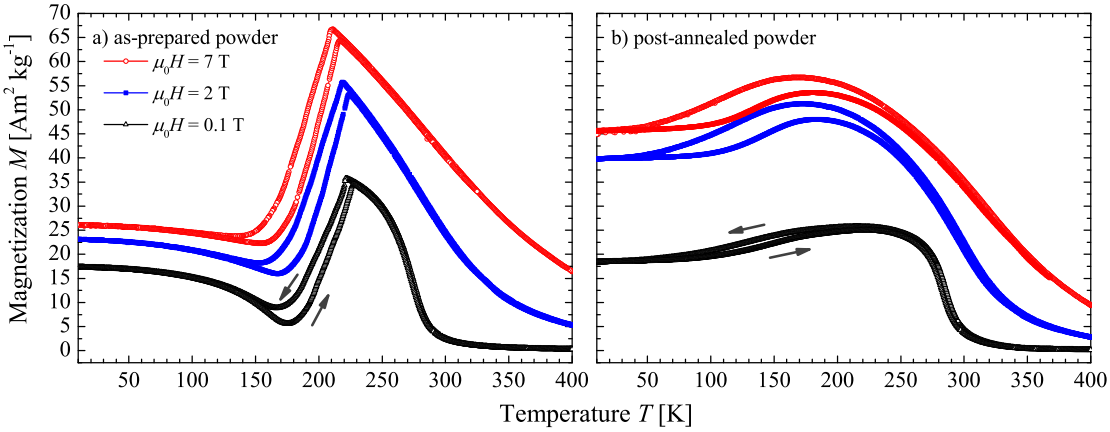

Figure 4. Temperature dependence of magnetization of $Mn_{50}Ni_{40}Sn_{10}$ in applied fields of μ_0H = 0.1, 2 and 7 T during heating and cooling modes for (**a**) as-prepared and (**b**) post-annealed powders.

Figure 4b displays the thermomagnetic curves of this alloy as a post-annealed powder using conditions similar to those of the as-prepared powder. Comparing both at μ_0H = 0.1 T, the martensitic transformation temperatures are very sensitive to the annealing method. Thus, M_s, M_f and T_M are decreasing, whereas T_C^A is increasing (for more details, see the Supplementary Information,Tables S1 and S2). Comparable results are known in Ni-rich Ni-and Mn-based Heusler alloys [19,20]. A similar feature has been found for Ni-Co-Mn-In alloys and is attributed to the modification of the atomic sites (order-disorder), the Mn-Mn distances and the Mn-Mn exchange coupling [47–50]. Additionally, based on this, the Fermi surface and the Brillouin zone boundary can be affected [50–53]. Therefore, for the post-annealed powder, the magnetization change during the martensitic transformation is decreased by one-third and remains constant with increasing μ_0H up to 7 T, indicating similar magnetic order of the martensite and austenite, *i.e.*, ferromagnetism.

At μ_0H = 0.1 T, ΔT_{Hyst} is increased significantly by 17 K, which is comparable to Ni-rich Ni- and Mn-based Heusler alloys [11,14]. However, for Ni-rich Ni-Mn-Sn Heusler alloys reported by Schlagel, McCallum and Lograsso [19] and Xuan *et al.* [20], the effect of annealing increased the magnetization change during the martensitic transformation. This was also observed for Ni-rich Ni-Mn-Co-In Heusler alloys, reported by Ito *et al.* [47]. Therefore, the impact of atomic ordering on annealing in terms of the martensitic transformation are different between Mn-rich Ni- and Mn-based Heusler alloys because of atomic site occupation of the Ni and Mn atoms. A recently reported study of the crystal structure of Mn-rich $Mn_{1.8}Ni_{1.2}Sn$ by our group [54] identified the disorder on the Wyckoff positions $4d$ and $4c$, by Ni and Mn atoms and their effects on the magnetic and transport properties.

Concerning the temperature-dependent magnetization of $Mn_{50}Ni_{41}Sn_9$, shown in Figure 5a, a small variation in composition of 1 at% increases M_s, M_f and T_M to higher temperatures (see the Supplementary Information, Tables S3 and S4). Thus, at r.t., the martensite and austenite are found to be present, verifying the crystal structures of the as-prepared powders shown in Figures 2a and 3a as determined by XRD analysis at r.t.

Comparing the magnetization of the austenite and martensite during the martensitic transformation at μ_0H = 0.1 T, the differences are quite small, which means that the martensite shows paramagnetism

and the austenite orders antiferromagnetically. Thus, the main contribution during the martensitic transformation comes from the structural distortion. At $\mu_0 H$ = 2 T, the magnetization change reaches a value of 20 Am^2 kg^{-1}, showing a sharp martensitic transformation.

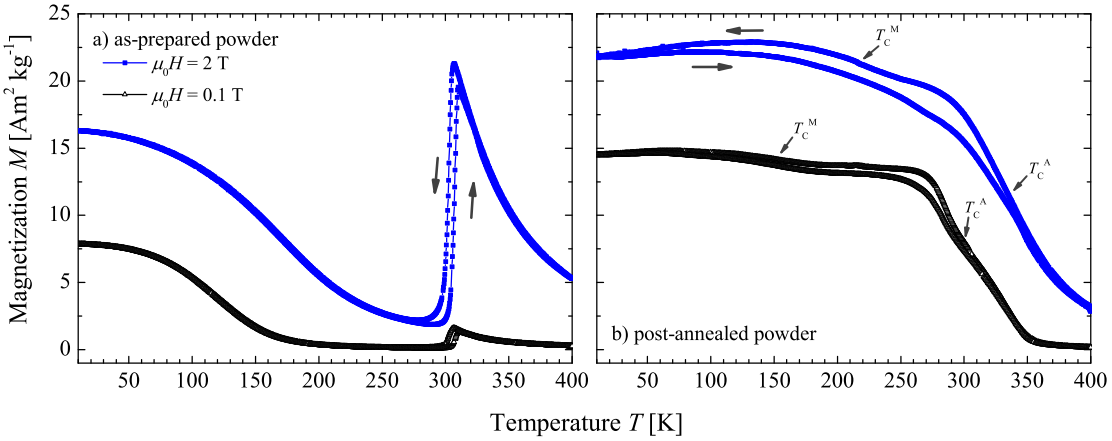

Figure 5. Temperature dependence of magnetization analysis of $Mn_{50}Ni_{41}Sn_9$ in applied fields of 0.1 and 2 T during heating and cooling for (**a**) as-prepared and (**b**) post-annealed powders.

As shown in Figure 5b, the temperature-dependent magnetization of the post-annealed powder is different from that of the as-prepared powder owing to a modified atomic site phenomena, which is verified by the variation of the crystal structures of both powders (see Figure 5).

However, for the post-annealed powder shown in Figure 5b, no clear magnetization change during the martensitic transformation was observed, indicating a similar magnetic coupling of the Mn atoms of the austenite and martensite. Additionally, the ferromagnetic ordering of the austenite increases, which indicates stabilization of the austenitic phase. Therefore, the martensitic transformation merges with T_C of the martensite and austenite. A similar phenomenon on the magnetization curve could be observed for Ni-Mn-Sn thin films [55]. The Curie temperatures of the austenite, T_C^A, and martensite, T_C^M, increase with increasing applied field from $\mu_0 H$ = 0.1 T to 2 T ($T^M_{C,0.1\ T}$ = 153 K *vs.* $T^M_{C,2\ T}$ = 217 K and $T^A_{C,0.1\ T}$ = 303 K *vs.* $T^A_{C,2\ T}$ = 331 K).

2.2. $Co_{50}Ni_{21}Ga_{32}$ Nanoparticles

2.2.1. Microscopic Analysis

Figure 6a,b shows the TEM micrograph and particle-size distribution, respectively, of the as-prepared $Co_{50}Ni_{21}Ga_{32}$ nanoparticles. The average particle size is 120 nm, with a broad size distribution in the range of 50–200 nm. As shown in Figure 6c, there are also some $Co_{50}Ni_{21}Ga_{32}$ nanorods and nanowires co-existing with the spherical nanoparticles.

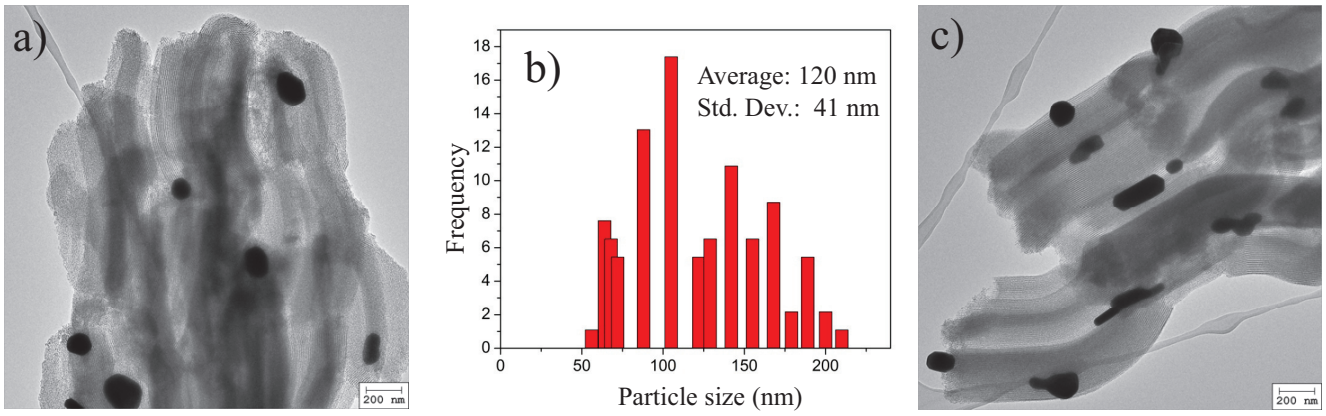

Figure 6. (**a**,**c**) TEM micrographs and (**b**) particle-size distribution of the as-prepared $Co_{50}Ni_{21}Ga_{32.5}$ nanoparticles CNG_AS.

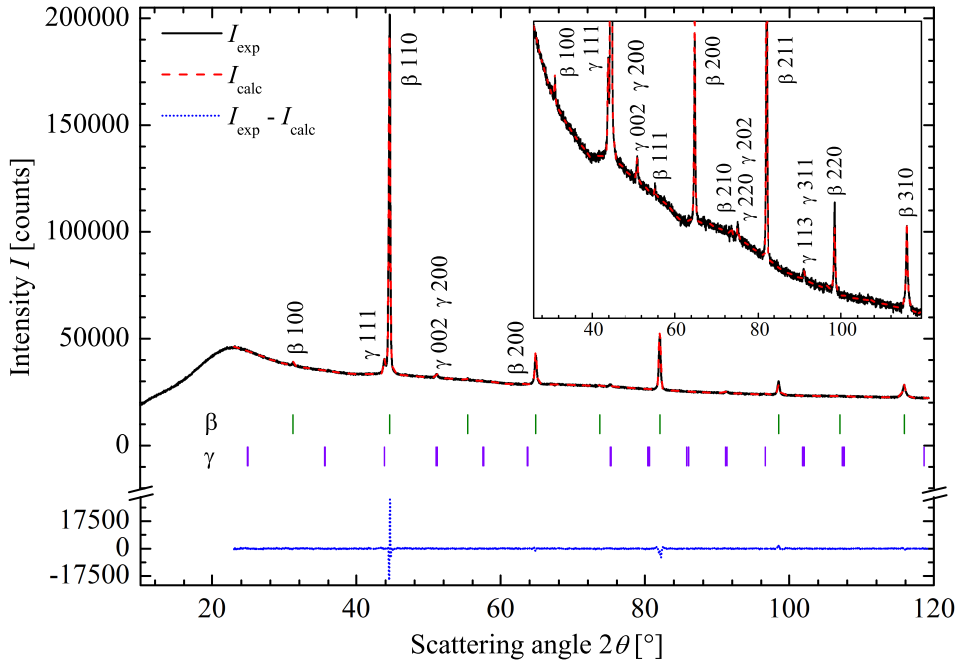

Figure 7. Experimental and the Rietveld-fitted XRD patterns of as-prepared $Co_{50}Ni_{21}Ga_{32}$ nanoparticles. The central-angle 2θ positions of the Bragg reflections according to the refined unit cell parameters of the phases are indicated by bars at the bottom. The difference curve is also shown at the bottom. Miller indices, hkl, of the selected observed reflections of the β ($B2$-type ordering) and γ phases are indicated. The inset shows the scaled XRD pattern for better visualization of the fitting of the weak reflections.

2.2.2. Crystal Structure of $Co_{50}Ni_{21}Ga_{32}$ Nanoparticles

Figures 7 and 8 show the XRD patterns of CNG_AS and CNG_AQ $Co_{50}Ni_{21}Ga_{32}$, respectively. The XRD-derived structural parameters (unit cell parameters, volume and weight content of the phases) and Rietveld fitting quality factors are compiled in Table 1. The XRD patterns exhibit an amorphous

halo due to the amorphous mesoporous SBA-15 silica. According to phase analysis and quantitative Rietveld fitting, two modifications with the Co_2NiGa nominal composition are present in the as-prepared nanoparticles (Figures 7). The main phase observed (94.5(1.6) wt% content) is a cubic β phase with a $B2$ partial ordering ($Pm\bar{3}m$, sg: 221, Inorganic Crystal Structure Database (ICSD) Code 169729 [35]) and a unit cell parameter of a = 2.8752(1) Å. As a minor phase with a content of 5.5(1.1) wt%, a fully-ordered γ phase with a slightly tetragonally distorted structure ($P/4mmm$, sg: 123, ICSD Code 157788 [34]) and unit cell parameters of a = 3.580(3) Å and c = 3.567(5) Å is detected (Table 1). In the β Co_2NiGa structure with $B2$-type ordering, the Ni and Ga atoms occupy the same position, whereas in the tetragonal γ-phase, different atoms are placed in different positions [34,35] and the unit cell volume is approximately two-times larger than that of the β phase. The $B2$-type ordering in the β phase is clearly indicated by the presence of the weak reflection, with Miller indices hkl = 100 at $2\theta = 31.12°$ and the distinct absence of the superlattice reflection at $2\theta = 26.87°$, which is characteristic of the β-phase with $L2_1$ atomic ordering (hkl = 111 for the $L2_1$-type β-structure).

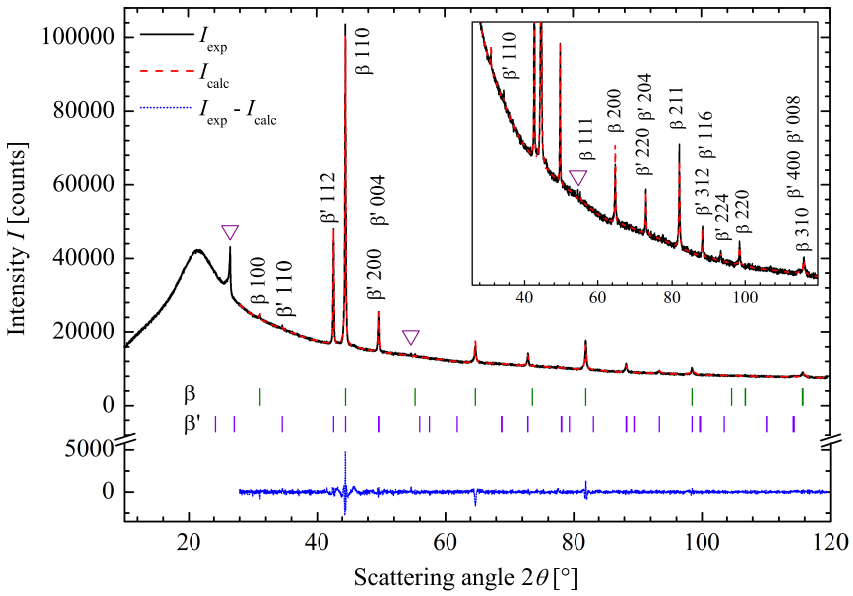

Figure 8. Experimental and Rietveld-fitted XRD patterns of annealed/quenched $Co_{50}Ni_{21}Ga_{32}$ nanoparticles. The central-angle 2θ positions of the Bragg reflections according to refined unit cell parameters of the phases are indicated by bars at the bottom. The difference curve is also shown at the bottom. Miller indices hkl of the selected observed reflections of the β ($B2$-type ordering) and β' phases are indicated. The inset shows the scaled XRD pattern for better visualization of the weak reflections. Non-indexed reflections are marked by triangles (probably 112 and 224 reflections of the Ga_7Ni_3 phase).

As shown in Figure 8, considerable changes occur in the crystalline phase composition and content after heat treatment. The minor tetragonal γ-phase disappears, and the content of the $B2$-type ordered Co_2NiGa β-phase decreases to 72.2(1.4) wt%, whereas its unit cell parameter increases to a = 2.8763(1) Å. The formation of a rather large amount of the highly ordered Co_2NiGa martensite phase (β') is observed (27.8(3.5) wt%) according to the results of the Rietveld quantitative analysis. In

the β'-phase (sg: 139, $I/4mmm$, ICSD Code 169733 [35]), the Co, Ni and Ga atoms are placed in different atomic positions, similar to what occurs in the γ-phase, but with approximately twice the unit cell volume, owing to the two-times larger tetragonal unit cell parameter c. Recently, the structure of the Co_2NiGa (β') phase was theoretically predicted [35] by means of density functional theory (DFT) calculations. According to Arróyave *et al.* [35], the tetragonal Co_2NiGa (β') phase exhibits the greatest structural stability among Co_2NiGa modifications. Thus, annealing results in a partial $\beta \longrightarrow \beta$' phase transformation from the partially ordered β phases ($B2$-type of ordering) to the highly ordered tetragonal β' that has a unit cell volume approximately four-times larger than that of the β phase. The presence of the different Co_2NiGa phases (β, β' and γ) is confirmed experimentally by the good quality of the Rietveld fitting of the XRD patterns (Figures 7 and 8) reflected in small values of the fitting agreement factors and structural Bragg factors (see Table 1).

Table 1. Structural parameters (unit cell parameters and weight content of the phases) and the Rietveld fitting quality factors of $Co_{50}Ni_{21}Ga_{32}$ nanoparticles. The estimated standard deviations (e.s.d.s) are indicated in round brackets.

ID	Phase	Space Group	Unit Cell Parameters		Wt Fraction [a] (wt%)	Rietveld Fitting Quality Factors			
			a (Å)	c (Å)		R_{wp} [b] (%)	cR_{wp} [c] (%)	R_B [d] (%)	$M_{e.s.d}$ [e]
CNG_AS	β	$Pm\bar{3}m$	2.8752(1)	a	94.5(1.6)	1.73	15.25	2.10	3.14
	γ	$P4/mmm$	3.580(3)	3.567(5)	5.5(1.1)			6.85	
CNG_AQ	β	$Pm\bar{3}m$	2.8763(1)	a	72.2(1.4)	1.26	10.56	2.12	2.46
	β'	$P4/mmm$	3.6691(4)	7.331(2)	27.8(3.5)			6.26	

[a] the amorphous SBA-15 phase and non-identified crystalline phase (for CNG_AQ) are not taken into account; [b] weighted profile factor; [c] background-corrected weighted profile factor; [d] Bragg factor; [e] Berrar's factor.

The crystallite size was analyzed using the Scherrer equation. It was revealed that the crystallite size of the β ($B2$-ordered) phase (D = 45(8) nm) is larger than that of its γ counterpart (D = 33(6) nm) for CNG_AS, whereas annealing resulted in crystallites of nearly the same size for the β ($B2$-type ordered) and β' crystallites, *i.e.*, 54 nm. The crystallite size of the unknown phase in CNG_AQ was D = 69(16) nm. A comparison with TEM results shows that the $Co_{50}Ni_{21}Ga_{32}$ nanoparticles are composed of either two or three nanocrystallites. This fact shows that the crystallite size derived from powder XRD analysis corresponds to the size of the coherent domains and not that of the particles observed by TEM.

2.2.3. Magnetism of the $Co_{50}Ni_{21}Ga_{32}$ Alloys

The magnetic properties of $Co_{50}Ni_{21}Ga_{32}$ nanoparticles changed significantly after annealing and quenching. As shown in Figure 9, large differences are observed in the thermomagnetic behavior of the two samples. The field-cooling (FC) and field-heating (FH) curves of the CNG_AS sample are dissimilar, and the divergence is visible across the entire measured temperature range. The origin of

the observed anomaly is unclear, but it is expected to be unrelated to the martensite transformation, since a transformation hysteresis was not observed. It is also probably associated with the presence of the γ phase, because a similar thermomagnetic feature was observed in $Co_{50}Ni_{21}Ga_{32}$ nanoparticles of a single γ phase. Further investigations are required to clarify this point. In comparison, the FC and FH curves of the CNG_AQ sample almost match, indicating the absence of martensite transformation across the measured temperature range. As pointed out by Brown [32], the martensite transformation in Co-Ni-Ga alloys does not occur abruptly, and it normally covers a broad temperature interval (even larger than 200 K). Therefore, in addition to the low weight fraction of the $Co_{50}Ni_{21}Ga_{32}$ phase in the nanoparticles, it is expected that thermomagnetic measurements might not be appropriate for probing the martensitic transformation in shape memory Heusler nanoparticles, such as $Co_{50}Ni_{21}Ga_{32}$. Instead, temperature-dependent XRD or neutron diffraction analysis might be a more suitable method. Furthermore, the magnetization of the CNG_AQ sample was much lower than that of the CNG_AS sample. This might be due to the absence of a γ phase after annealing, which contributes significantly to the magnetization of the two-phase $Co_{50}Ni_{21}Ga_{32}$ nanoparticles.

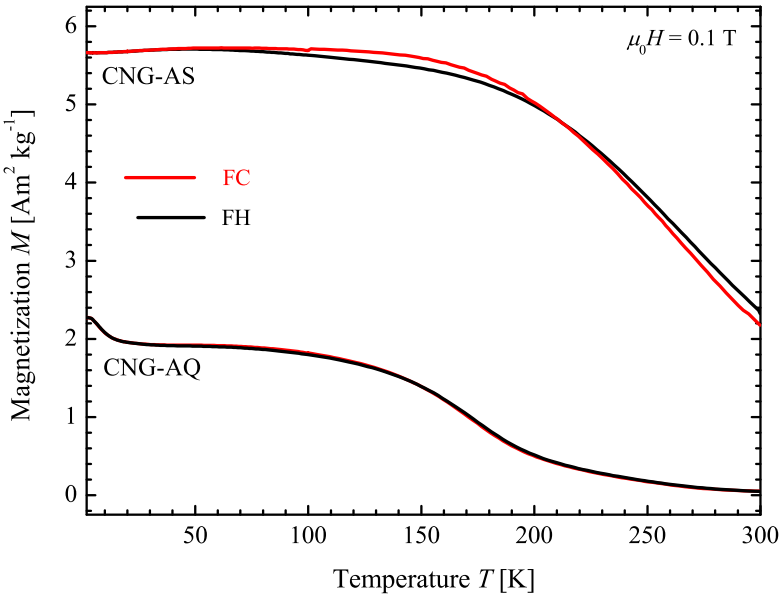

Figure 9. Temperature-dependent magnetization (M - T) curves of $Co_{50}Ni_{21}Ga_{32}$ nanoparticles before and after annealing. FC, field cooling; FH, field heating. Applied magnetic field: 0.1 T.

3. Materials and Methods

3.1. Experimental Details of the $Mn_{50}Ni_{40}Sn_{10}$ and $Mn_{50}Ni_{41}Sn_9$ Alloys

Bulk $Mn_{50}Ni_{40}Sn_{10}$ and $Mn_{50}Ni_{41}Sn_9$ alloys with a total mass of 5 g were prepared by inductive melting of the elements (Ni foil, 99.9%, ChemPur; Mn pieces, 99.99%, ChemPur; Sn granules, 99.999%, ChemPur) in Al_2O_3 crucibles (Ø = 10 mm, Friatec, Al23). The total mass loss was $\leq$ 1 wt%. A subsequent heat treatment for 3 weeks was performed by encapsulating the alloys in an arc-welded tantalum ampoule at 0.3 bar Ar and jacketing them in an evacuated fused quartz glass ampoule.

The $Mn_{50}Ni_{40}Sn_{10}$ sample was annealed at 973 K (onset of melting at T_o = 1188 K from DSC analysis) and the $Mn_{50}Ni_{41}Sn_9$ sample at 1073 K (T_o = 1,205 K). Lastly, both alloys were quenched in ice-water by shattering the silica ampoule.

For post-annealing, the powders were ground in a WC/Co mortar and an agate mortar and sieved to grain sizes, d, of $\leq$ 50 μm for $Mn_{50}Ni_{40}Sn_{10}$ and 100 μm for $Mn_{50}Ni_{41}Sn_9$. Subsequently, the powders were enclosed in an arc-welded tantalum ampoule at 0.3 bar Ar, which, in turn, was jacketed by an evacuated fused quartz glass ampoule. Finally, both ampoules were annealed for 24 h at 873 K and cooled to r.t. over 48 h.

To characterize the alloys, powder XRD measurements were performed at r.t. using an image-plate Huber G670 Guinier camera, Rimsting, Germany equipped with a Ge(111) monochromator. The compounds were analyzed by using Cu-$K\alpha_1$ radiation ($\lambda = 1.540598$ Å) in the range $10° \leq \theta \leq 100°$. A small amount of powder was homogeneously dispersed on Mylar foil. The WinXPOW package [56] was used to determine the lattice parameters. The Le Bail fitting was carried out by Jana, 2006 [57].

Thermal analysis was performed with a differential scanning calorimeter (DSC/TG Netzsch STA 449C, Selb, Germany) at a heating rate of 10 K/min from r.t. to a maximum temperature of 1673 K.

ICP-OES by means of a spectrometer VISTA (Varian Inc., Palo Alto, CA, USA) was used to analyze the final composition after annealing. Chemical analysis by EDXS was performed, and SEM images of secondary electrons and back-scattered electrons were taken using a Philips XL30 system, (SEMTech Solutions, Amsterdam, The Netherlands) with a LaB_6 cathode and an XFLASH® detector, (Bruker, Billerica, MA, USA) at 15 kV. Wavelength dispersive X-ray spectroscopy analysis was done using a Cameca SX-100 electron probe analyzer, (CAMECA, Gennevilliers, France) and elemental standards.

Magnetic properties were investigated by means of a commercial system (VSM, quantum design, San Diego, CA, USA). The temperatures for the magnetic properties measurements were in the range from 1.8 to 400 K.

3.2. Experimental Details of the $Co_{50}Ni_{21}Ga_{32}$ Nanoparticles

All chemicals were purchased from Sigma-Aldrich, (St. Louis, MO, USA) or Alfa Aesar, (Ward Hill, MA, USA) and used as-received. The nonionic triblock copolymer, Pluronic P123 (MW 5800), and tetraethoxysilane (TEOS) were used as a structure-directing surfactant and silicon source, respectively. Furthermore, the precursors for the $Co_{50}Ni_{21}Ga_{32}$ nanocrystals were $CoCl_2 \times 6H_2O$ (99.9%), $Ni(NO_3)_2 \times 6H_2O$ (99.999%) and $Ga(NO_3) \times H_2O$ (99.9%).

First, mesoporous SBA-15 silica was prepared as the template for the $Co_{50}Ni_{21}Ga_{32}$ nanoparticles. Four grams of Pluronic P123 were dissolved into a solution consisting of 30 g of water and 120 mL of 2 M HCl at 310 K and stirred overnight. Subsequently, 8.5 g of TEOS was vigorously stirred for 24 h into the clear solution at the aforementioned temperature. The milky suspension was then transferred to a 250-mL polypropylene storage bottle and hydrothermally treated at 353 K for 24 h. The solid product was recovered, washed with deionized water and air-dried at r.t. in the chemical hood. The dried SBA-15 powders were then slowly heated at 1 K/min to 773 K and annealed for 6 h in order to remove the structure-directing agents.

The $Co_{50}Ni_{21}Ga_{32}$ nanoparticles were prepared using 1 g of SBA-15 as the template. The amounts of precursor salts were 0.234 g (0.98 mmol) of $CoCl_2 \times 6H_2O$, 0.144 g (0.49 mmol) of $Ni(NO_3)_2 \times 6H_2O$ and 0.22 g (0.65 mmol) of $Ga(NO_3) \times H_2O$. First, the precursor salts were dissolved in 50 mL of methanol and then mildly ultrasonically vibrated for 10 min. Subsequently, 1 g of SBA-15 silica was added to the precursor solution, and the suspension was ultrasonically vibrated for another 20 min. The methanol was removed by a rotor evaporator, and the dried powder (200 mg) was heated at 10 K/min, under H_2 atmosphere to 1123 K and held at this temperature for 6 h.

The chemical composition of $Co_{50}Ni_{21}Ga_{32}$ and the metal-to-silica weight ratios were obtained by a chemical analysis method using ICP-OES by means of the VISTA spectrometer (Varian Inc., Palo Alto, CA, USA). The as-prepared Co-Ni-Ga nanoparticles were found to have a $Co_{50}Ni_{21}Ga_{32}$ composition, and the weight fraction of $Co_{50}Ni_{21}Ga_{32}$ in the $Co_{50}Ni_{21}Ga_{32}$/silica nanocomposites was 13.45 wt%.

Suspensions of SBA-15-supported $Co_{50}Ni_{21}Ga_{32}$ nanoparticles were used for TEM sample preparation. Several drops of the suspensions were loaded onto a carbon-coated copper grid and transferred to the microscope after being completely dried. The average particle size was evaluated by counting more than 100 individual particles. A Tecnai 10 TEM system (FEI, Eindhoven, The Netherlands) equipped with a LaB_6-source at an acceleration voltage of 100 kV was used to investigate particle morphology, size distribution and electron diffraction. Images were recorded with a F224HD 2k slow-scan charge-coupled device (CCD) camera (Tietz Video and Image Processing Systems, Gauting, Germany).

The crystal structure of the $Co_{50}Ni_{21}Ga_{32}$/SBA-15 nanocomposite system was investigated by powder XRD technique. An X'Pert PRO diffractometer designed in Bragg–Brentano geometry and supplied with a solid-state X'Celerator linear detector was used (PANalytical B.V., Almelo, The Netherlands). The Cu-$K\alpha_1$-radiation of the Cu anode of the X-ray tube ($\lambda = 1.540598$ Å) monochromatized by a primary Johansson-type Ge(111) monochromator was utilized. Additionally, XRD measurements of the powder samples mixed with the Si 640c powder internal standard (National Institute of Standards, Gaithersburg, MD, USA) were performed. The recorded XRD patterns of the samples were corrected to the $\Delta 2\theta_{zero}$ shift using these data as an external standard. The contribution of the substrate was corrected by subtracting the XRD pattern of the substrate measured with high counting statistics.

The microstructure calculations for $Co_{50}Ni_{21}Ga_{32}$ samples were carried out by means of the program $SIZECR$ [58]. First, an appropriate correction of the instrumental broadening according to the pseudo-Voigt profile type of the reflections observed [59] was performed. The inconsistency of the observed XRD reflection broadening with the presence of the microstrains in the $Co_{50}Ni_{21}Ga_{32}$ crystallites was established. Finally, the average sizes of XRD crystallites of the $Co_{50}Ni_{21}Ga_{32}$ phases were calculated from Scherrer's equation assuming zero microstrain contribution.

Using the recorded XRD patterns and ICSD [60], the phase analysis was carried out. To confirm the results of the phase analysis and to obtain the quantitative characteristics of the observed crystalline phases, Rietveld fitting of the XRD patterns was carried out by means of the Rietveld program $WinCSD$ [61]. The weight scheme $w_i = 1/y_i$ was used in the Rietveld fitting, where y_i is the intensity recorded at the 2θ-step i of the XRD pattern. The isotropic overall temperature factors $B_{\mathrm{iso,overall}}$ of the atoms were refined for each phase. To neglect the contribution of the amorphous SiO_2 (SBA-15), the XRD patterns were cut at diffraction angles 2θ of less than 23°, where no XRD reflections of the

crystalline phases were observed. At higher angles, the residual amorphous contribution was modeled by a background function. The estimated standard deviations (e.s.d.s) of the crystalline phase parameters were obtained in the Rietveld refinement and were underestimated owing to serial correlations. These were corrected by multiplication on the correcting coefficients, $M_{e.s.d.}$ (see Table 1), calculated by means of Berrar's procedure [62] implemented in $WinCSD$.

Additionally, for the CNG_AQ sample, two non-indexed reflections of an unknown phase were detected at 2θ = 25.88° and 53.22° (marked by triangles in Figure 8). The first one is more intensive, whereas the second one is very weak. According to the 2θ values, these reflections can be attributed to an intermetallic phase with a nominal composition of Ga_7Ni_3 ($Immm$, space group No. 229, ICSD Code 408313 [63]) with a calculated unit cell parameter of a = 8.225(4) Å. This phase is probably characterized by a highly preferred orientation along [112], resulting in the observation of only the two reflections mentioned above (with hkl = 112 and 224, respectively). Owing to a small amount of this phase and the limited number of the reflections observed, attempts to take this phase into account during the Rietveld fitting failed. Finally, for the CNG_AQ sample, the cutting was done at $2\theta = 28°$ in order to exclude the contribution of the most intensive reflection of this phase.

In order to investigate the magnetic properties of $Co_{50}Ni_{21}Ga_{32}$ nanoparticles before and after annealing, temperature-dependent magnetization ($M-T$) measurements were conducted. These measurements were performed under a small magnetic field of 0.1 T from 300 to 1.8 K (field cooling) and then from 1.8 to 300 K (field heating) using the commercial magnetometers Quantum Design MPMS-XL-7 and MPMS-3. The actual magnetization of the $Co_{50}Ni_{21}Ga_{32}$ nanoparticles was calculated based on the weight fraction of the nanoparticles in the nanocomposites. The nanoparticle samples were fixed in a quartz capillary with molten paraffin wax in order to avoid unwanted sample movement during the measurements.

4. Conclusions

In conclusion, we studied the effect of annealing on powdered $Mn_{50}Ni_{40}Sn_{10}$ and $Mn_{50}Ni_{41}Sn_9$ alloys and on $Co_{50}Ni_{21}Ga_{32}$ nanoparticles. Concerning the as-prepared powders of $Mn_{50}Ni_{40}Sn_{10}$ and $Mn_{50}Ni_{41}Sn_9$, a slight change in the Sn-content increased the martensitic transformation temperatures, resulting in an austenitic phase for $Mn_{50}Ni_{40}Sn_{10}$ and a martensitic phase for $Mn_{50}Ni_{41}Sn_9$ at r.t. The annealing of both alloys resulted in changes to the crystal structure of the martensite of $Mn_{50}Ni_{41}Sn_9$ owing to a stabilization of the austenitic phase. It also resulted in a decrease of the martensitic transformation temperatures and an increase in the thermal hysteresis during the martensitic transformation. This might be associated with a release of stress during the annealing process.

We also investigated the annealing effect on $Co_{50}Ni_{21}Ga_{32}$ nanoparticles. XRD analysis showed the absence of a martensitic phase in the as-prepared $Co_{50}Ni_{21}Ga_{32}$ nanoparticles at r.t. After the heat treatment, a martensitic phase with a tetragonal crystal structure formed together with a parent austenitic phase. Thermomagnetic measurements revealed a pronounced decrease in magnetization of the annealed nanoparticles, which is consistent with the variations of the crystal structure. The intrinsic features in the martensite transformation of $Co_{50}Ni_{21}Ga_{32}$ compounds make it difficult to probe the phase transition by temperature-dependent magnetic measurements.

Acknowledgments

This work was financially supported by the ERC Advanced Grant No. 291472 "Idea Heusler" and DFG Project No. 1.2-A in the research unit FOR 1464 ASPIMATT. Additionally, the contributions of S. Kostmann (microstructure analysis), S. Scharsach (DSC/TG), U. Schmidt, A. Völzke and S. Schwinger (ICP-OES) are gratefully acknowledged.

Author Contributions

Tina Fichtner and Changhai Wang performed the synthesis of the alloys $Mn_{50}Ni_{40}Sn_{10}$ and $Mn_{50}Ni_{41}Sn_9$ or $Co_{50}Ni_{21}Ga_{32}$, respectively. Aleksandr A. Levin carried out the XRD measurements of the $Co_{50}Ni_{21}Ga_{32}$ samples for Rietveld fitting and performed quantitative analysis and crystallite size calculations. Guido Kreiner characterized the $Mn_{50}Ni_{40}Sn_{10}$ and $Mn_{50}Ni_{41}Sn_9$ alloys. Catalina Salazar Mejia analyzed the magnetic properties of the $Mn_{50}Ni_{40}Sn_{10}$ and $Mn_{50}Ni_{41}Sn_9$ alloys. Simone Fabbrici and Franca Albertini discussed the analysis and the results. Claudia Felser supervised the work and discussed the results and the analysis with the other authors.

Conflicts of Interest

The authors declare no conflict of interest.

References

1. Ullakko, K.; Huang, J.K.; Kantner, C.; O'Handley, R.C.; Kokorin, V.V. Large magnetic-field-induced strains in Ni_2MnGa single crystals. *Appl. Phys. Lett.* **1996**, *69*, 1966–1968.
2. Brück, E. Developments in magnetocaloric refrigeration. *J. Phys. D Appl. Phys.* **2005**, *38*, R381–R391.
3. Planes, A.; Manosa, L.; Acet, M. Magnetocaloric effect and its relation to shape-memory properties in ferromagnetic Heusler alloys. *J. Phys. Condes. Matter* **2009**, *21*, 233201:1–233201:29.
4. Buchelnikov, V.D.; Sokolovskiy, V.V. Magnetocaloric effect in Ni-Mn-X (X = Ga, In, Sn, Sb) Heusler alloys. *Phys. Met. Metallogr.* **2011**, *112*, 633–665.
5. Franco, V.; Blázquez, J.; Ingale, B.; Conde, A. The Magnetocaloric Effect and Magnetic Refrigeration Near Room Temperature: Materials and Models. *Annu. Rev. Mater. Res.* **2012**, *42*, 305–342.
6. Roy, S.B. Chapter two—Magnetocaloric effect in intermetallic compounds and alloys. In *Handbook of Magnetic Materials*; Buschow, K., Ed.; Elsevier: Amsterdam, The Netherlands, 2014; Volume 22, pp. 203–316.
7. Sozinov, A.; Likhachev, A.A.; Lanska, N.; Ullakko, K. Giant magnetic-field-induced strain in NiMnGa seven-layered martensitic phase. *Appl. Phys. Lett.* **2002**, *80*, 1746–1748.
8. Müllner, P.; Chernenko, V.; Kostorz, G. Large magnetic-field-induced deformation and magneto-mechanical fatigue of ferromagnetic Ni-Mn-Ga martensites. *Mater. Sci. Eng. A* **2004**, *387–389*, 965–968.

9. Koyama, K.; Okada, H.; Watanabe, K.; Kanomata, T.; Kainuma, R.; Ito, W.; Oikawa, K.; Ishida, K. Observation of large magnetoresistance of magnetic Heusler alloy $Ni_{50}Mn_{36}Sn_{14}$ in high magnetic fields. *Appl. Phys. Lett.* **2006**, *89*, 182510:1–182510:3.
10. Yu, S.Y.; Liu, Z.H.; Liu, G.D.; Chen, J.L.; Cao, Z.X.; Wu, G.H.; Zhang, B.; Zhang, X.X. Large magnetoresistance in single-crystalline $N_{50}Mn_{50-x}In_x$ alloys (x = 14 – 16) upon martensitic transformation. *Appl. Phys. Lett.* **2006**, *89*, 162503:1–162503:3.
11. Krenke, T.; Duman, E.; Acet, M.; Wassermann, E.F.; Moya, X.; Manosa, L.; Planes, A. Inverse magnetocaloric effect in ferromagnetic Ni-Mn-Sn alloys. *Nat. Mater.* **2005**, *4*, 450–454.
12. Han, Z.D.; Wang, D.H.; Zhang, C.L.; Tang, S.L.; Gu, B.X.; Du, Y.W. Large magnetic entropy changes in the $Ni_{45.4}Mn_{41.5}In_{13.1}$ ferromagnetic shape memory alloy. *Appl. Phys. Lett.* **2006**, *89*, 182507:1–182507:3.
13. Liu, J.; Gottschall, T.; Skokov, K.; Moore, J.; Gutfleisch, O. Giant magnetocaloric effect driven by structural transitions. *Nat. Mater.* **2012**, *11*, 620–626.
14. Han, Z.D.; Wang, D.H.; Zhang, C.L.; Xuan, H.C.; Gu, B.X.; Du, Y.W. Low-field inverse magnetocaloric effect in $Ni_{50-x}Mn_{39+x}Sn_{11}$ Heusler alloys. *Appl. Phys. Lett.* **2007**, *90*, 042507:1–042507:3.
15. Ma, L.; Wang, W.H.; Lu, J.B.; Li, J.Q.; Zhen, C.M.; Hou, D.L.; Wu, G.H. Coexistence of reentrant-spin-glass and ferromagnetic martensitic phases in the $Mn_2Ni_{1.6}Sn_{0.4}$ Heusler alloy. *Appl. Phys. Lett.* **2011**, *99*, 182507:1–182507:3.
16. Wu, Z.; Liu, Z.; Yang, H.; Liu, Y.; Wu, G. Martensitic and magnetic transformation behaviours in $Mn_{50}Ni_{42-x}Sn_8Co_x$ polycrystalline alloys. *J. Phys. D Appl. Phys.* **2011**, *44*, 385403:1–385403:7.
17. Ghosh, A.; Mandal, K. Large magnetic entropy change and magnetoresistance associated with a martensitic transition of Mn-rich $Mn_{50.5-x}Ni_{41}Sn_{8.5+x}$ alloys. *J. Phys. D Appl. Phys.* **2013**, *46*, 435001:1–435001:7.
18. Ma, L.; Wang, S.Q.; Li, Y.Z.; Zhen, C.M.; Hou, D.L.; Wang, W.H.; Chen, J.L.; Wu, G.H. Martensitic and magnetic transformation in $Mn_{50}Ni_{50-x}Sn_x$ ferromagnetic shape memory alloys. *J. Appl. Phys.* **2012**, *112*, 083902:1–083902:4.
19. Schlagel, D.L.; McCallum, R.W.; Lograsso, T.A. Influence of solidification microstructure on the magnetic properties of Ni-Mn-Sn Heusler alloys. *J. Alloys Compd.* **2008**, *463*, 38–46.
20. Xuan, H.C.; Xie, K.X.; Wang, D.H.; Han, Z.D.; Zhang, C.L.; Gu, B.X.; Du, Y.W. Effect of annealing on the martensitic transformation and magnetocaloric effect in $Ni_{44.1}Mn_{44.2}Sn_{11.7}$ ribbons. *Appl. Phys. Lett.* **2008**, *92*, 242506:1–242506:3.
21. Oikawa, K.; Ota, T.; Ohmori, T.; Tanaka, Y.; Morito, H.; Fujita, A.; Kainuma, R.; Fukamichi, K.; Ishida, K. Magnetic and martensitic phase transitions in ferromagnetic Ni-Ga-Fe shape memory alloys. *Appl. Phys. Lett.* **2002**, *81*, 5201–5203.
22. Liu, Z.H.; Zhang, M.; Cui, Y.T.; Zhou, Y.Q.; Wang, W.H.; Wu, G.H.; Zhang, X.X.; Xiao, G. Martensitic transformation and shape memory effect in ferromagnetic Heusler alloy Ni_2FeGa. *Appl. Phys. Lett.* **2003**, *82*, 424–426.
23. Hamilton, R.; Efstathiou, C.; Sehitoglu, H.; Chumlyakov, Y. Thermal and stress-induced martensitic transformations in NiFeGa single crystals under tension and compression. *Scr. Mater.* **2006**, *54*, 465–469.

24. Oikawa, K.; Wulff, L.; Iijima, T.; Gejima, F.; Ohmori, T.; Fujita, A.; Fukamichi, K.; Kainuma, R.; Ishida, K. Promising ferromagnetic Ni-Co-Al shape memory alloy system. *Appl. Phys. Lett.* **2001**, *79*, 3290–3292.
25. Karaca, H.; Karaman, I.; Lagoudas, D.; Maier, H.; Chumlyakov, Y. Recoverable stress-induced martensitic transformation in a ferromagnetic CoNiAl alloy. *Scr. Mater.* **2003**, *49*, 831–836.
26. Wuttig, M.; Li, J.; Craciunescu, C. A new ferromagnetic shape memory alloy system. *Scr. Mater.* **2001**, *44*, 2393–2397.
27. Liu, J.; Xia, M.; Huang, Y.; Zheng, H.; Li, J. Effect of annealing on the microstructure and martensitic transformation of magnetic shape memory alloys CoNiGa. *J. Alloys Compd.* **2006**, *417*, 96–99.
28. Dai, X.F.; Liu, G.D.; Liu, Z.H.; Wu, G.H.; Chen, J.L.; Meng, F.B.; Liu, H.Y.; Yan, L.Q.; Qu, J.P.; Li, Y.X.; *et al*. Superelasticity of CoNiGa:Fe single crystals. *Appl. Phys. Lett.* **2005**, *87*, 112504:1–112504:3.
29. Dogan, E. Co-Ni-Ga High Temperature Shape Memory Alloys. Master's Thesis, Texas A&M University, College Station, TX, USA, 2010.
30. Sato, M.; Okazaki, T.; Furuya, Y.; Wuttig, M. Magnetostrictive and Shape Memory Properties of Heusler Type Co_2NiGa Alloys . *Mater. Trans.* **2003**, *44*, 372–376.
31. Sato, M.; Okazaki, T.; Furuya, Y.; Kishi, Y.; Wuttig, M. Phase transformation and magnetic property of heusler type Co_2NiGa alloys. *Mater. Trans.* **2004**, *45*, 204–207.
32. Brown, P.J.; Ishida, K.; Kainuma, R.; Kanomata, T.; Neumann, K.U.; Oikawa, K.; Ouladdiaf, B.; Ziebeck, K.R. Crystal structures and phase transitions in ferromagnetic shape memory alloys based on Co-Ni-Al and Co-Ni-Ga. *J. Phys. Condens. Matter* **2005**, *17*, 1301–1310.
33. Oikawa, K.; Ota, T.; Imano, Y.; Omori, T.; Kainuma, R.; Ishida, K. Phase equilibria and phase transformation of Co-Ni-Ga ferromagnetic shape memory alloy system. *J. Phase Equilib. Diffus.* **2006**, *27*, 75–82.
34. Dai, X.; Liu, G.; Li, Y.; Qu, J.; Li, J.; Chen, J.; Wu, G. Structure and magnetic properties of highly ordered Co_2NiGa alloys. *J. Appl. Phys.* **2007**, *101*, 09N503:1–09N503:3.
35. Arróyave, R.; Junkaew, A.; Chivukula, A.; Bajaj, S.; Yao, C.Y.; Garay, A. Investigation of the structural stability of Co_2NiGa shape memory alloys via ab initio methods. *Acta Mater.* **2010**, *58*, 5220–5231.
36. Dogan, E.; Karaman, I.; Chumlyakov, Y.; Luo, Z. Microstructure and martensitic transformation characteristics of CoNiGa high temperature shape memory alloys. *Acta Mater.* **2011**, *59*, 1168–1183.
37. Dadda, J.; Maier, H.; Karaman, I.; Karaca, H.; Chumlyakov, Y. Pseudoelasticity at elevated temperatures in [001] oriented $Co_{49}Ni_{21}Ga_{30}$ single crystals under compression. *Scr. Mater.* **2006**, *55*, 663–666.
38. Li, Y.X.; Liu, H.Y.; Meng, F.B.; Yan, L.Q.; Liu, G.D.; Dai, X.F.; Zhang, M.; Liu, Z.H.; Chen, J.L.; Wu, G.H.; *et al*. Magnetic field-controlled two-way shape memory in CoNiGa single crystals. *Appl. Phys. Lett.* **2004**, *84*, 3594–3596.
39. Sarma, S.; Srinivasan, A. Influence of Annealing Temperature on the Properties of Co-Ni-Ga Ferromagnetic Shape Memory Alloy. *Adv. Mater. Res.* **2008**, *52*, 63–68.

40. Dai, X.F.; Wang, H.Y.; Liu, G.D.; Wang, Y.G.; Duan, X.F.; Chen, J.L.; Wu, G.H. Effect of heat treatment on the properties of $Co_{50}Ni_{20}Ga_{30}$ ferromagnetic shape memory alloy ribbons. *J. Phys. D Appl. Phys.* **2006**, *39*, 2886–2889.
41. Liu, J.; Scheerbaum, N.; Hinz, D.; Gutfleisch, O. A high-temperature coupling of martensitic and magnetic transformations and magnetic entropy change in Ni-Fe-Ga-Co alloys. *Scr. Mater.* **2008**, *59*, 1063–1066.
42. Yu, S.; Yan, S.; Kang, S.; Tang, X.; Qian, J.; Chen, J.; Wu, G. Magnetic field-induced martensite-austenite transformation in Fe-substituted NiMnGa ribbons. *Scr. Mater.* **2011**, *65*, 9–12.
43. Tao, Q.; Han, Z.D.; Wang, J.J.; Qian, B.; Zhang, P.; Jiang, X.F.; Wang, D.H.; Du, Y.W. Phase stability and magnetic-field-induced martensitic transformation in Mn-rich NiMnSn alloys. *AIP Adv.* **2012**, *2*, 042181, doi:10.1063/1.4772626.
44. Khachaturyan, A.; Shapiro, S.; Semenovskaya, S. Adaptive phase formation in martensitic transformation. *Phys. Rev. B* **1991**, *43*, 10832–10843.
45. Kaufmann, S.; Rößler, U.K.; Heczko, O.; Wuttig, M.; Buschbeck, J.; Schultz, L.; Fähler, S. Adaptive Modulations of Martensites. *Phys. Rev. Lett.* **2010**, *104*, 145702:1–145702:4.
46. Li, Z. Study on Crystallographic Features of Ni-Mn-Ga Ferromagnetic Shape Memory Alloys. Ph.D. Thesis, University de Lorraine and Northeastern University, Metz, France, 10 September 2011.
47. Ito, W.; Nagasako, M.; Umetsu, R.Y.; Kainuma, R.; Kanomata, T.; Ishida, K. Atomic ordering and magnetic properties in the $Ni_{45}Co_5Mn_{36.7}In_{13.3}$ metamagnetic shape memory alloy. *Appl. Phys. Lett.* **2008**, *93*, 232503:1–232503:3.
48. Ito, W.; Ito, K.; Umetsu, R.Y.; Kainuma, R.; Koyama, K.; Watanabe, K.; Fujita, A.; Oikawa, K.; Ishida, K.; Kanomata, T.; *et al*. Kinetic arrest of martensitic transformation in the NiCoMnIn metamagnetic shape memory alloy. *Appl. Phys. Lett.* **2008**, *92*, 021908:1–021908:3.
49. Kustov, S.; Corró, M.L.; Pons, J.; Cesari, E. Entropy change and effect of magnetic field on martensitic transformation in a metamagnetic Ni-Co-Mn-In shape memory alloy. *Appl. Phys. Lett.* **2009**, *94*, 191901:1–191901:3.
50. Chen, L.; Hu, F.X.; Wang, J.; Shen, J.; Sun, J.R.; Shen, B.G.; Yin, J.H.; Pan, L.Q.; Huang, Q.Z. Effect of post-annealing on martensitic transformation and magnetocaloric effect in $Ni_{45}Co_5Mn_{36.7}In_{13.3}$ alloys. *J. Appl. Phys.* **2011**, *109*, 07A939:1–07A939:3.
51. Webster, P.J.; Ziebeck, K.R.A.; Town, S.L.; Peak, M.S. Magnetic order and phase transformation in Ni_2MnGa. *Philos. Mag. B* **1984**, *49*, 295–310.
52. Sato, H.; Toth, R. Effect of additional elements on the period of CuAu II and the origin of the long-period superlattice. *Phys. Rev.* **1961**, *124*, 1833–1847.
53. Entel, P.; Buchelnikov, V.D.; Khovailo, V.V.; Zayak, A.T.; Adeagbo, W.A.; Gruner, M.E.; Herper, H.C.; Wassermann, E.F. Modelling the phase diagram of magnetic shape memory Heusler alloys. *J. Phys. D Appl. Phys.* **2006**, *39*, 865–889.
54. Fichtner, T.; Kreiner, G.; Chadov, S.; Fecher, G.H.; Schnelle, W.; Hoser, A.; Felser, C. Magnetic and transport properties in the Heusler series $Ni_{2-x}Mn_{1+x}Sn$ affected by chemical disorder. *Intermetallics* **2015**, *57*, 101–112.

55. Auge, A.; Teichert, N.; Meinert, M.; Reiss, G.; Hütten, A.; Yüzüak, E.; Dincer, I.; Elerman, Y.; Ennen, I.; Schattschneider, P.; *et al*. Thickness dependence of the martensitic transformation, magnetism, and magnetoresistance in epitaxial Ni-Mn-Sn ultrathin films. *Phys. Rev. B* **2012**, *85*, 214118:1–214118:8.
56. *STOE WinXPOW*, Version 2.25; Stoe & Cie GmbH: Darmstadt, Germany, 2009.
57. *Jana2006*; Institute of Physics: Praha, Czech Republic, 2006.
58. Levin, A.A.; Levichkova, M.; Hildebrandt, D.; Klisch, M.; Weiss, A.; Wynands, D.; Elschner, C.; Pfeiffer, M.; Leo, K.; Riede, M.; *et al*. Effect of film thickness, type of buffer layer, and substrate temperature on the morphology of dicyanovinyl-substituted sexithiophene films. *Thin Solid Films* **2012**, *520*, 2479–2487.
59. Rehani, B.R.; Joshi, P.B.; Lad, K.N.; Pratap, A. Crystallite size estimation of elemental and composite silver nano-powders using XRD principles. *Indian J. Pure Appl. Phys.* **2006**, *44*, 157–161.
60. Belsky, A.; Lynn, V. Research papers New developments in the Inorganic Crystal Structure Database (ICSD): Accessibility in support of materials research and design research papers. *Acta Cryst. B* **2002**, *58*, 364–369.
61. Akselrud, L.; Grin, Y. WinCSD : Software package for crystallographic calculations (Version 4). *J. Appl. Cryst.* **2014**, *47*, 803–805.
62. Bérar, J.F.; Lelann, P. E.s.d.'s and estimated probable error obtained in Rietveld refinements with local correlations. *J. Appl. Crystallogr.* **1991**, *24*, 1–5.
63. Häussermann, U.; Elding-ponte, M.; Svensson, C.; Lidin, S. Compounds with the Ir_3Ge_7 structure type : Interpenetrating frameworks with flexible Bonding Properties. *Chem. Eur. J.* **1998**, *4*, 1007–1015.